Nanostructuring surfaces by ion sputtering

2002 J. Phys.: Condens. Matter 14 8153

(http://iopscience.iop.org/0953-8984/14/35/301)

INSTITUTE OF PHYSICS PUBLISHING JOURNAL OF PHYSICS: CONDENSED MATTER

J. Phys.: Condens. Matter **14** (2002) 8153–8175 PII: S0953-8984(02)32767-X

Nanostructuring surfaces by ion sputtering

U Valbusa[1], **C Boragno and F Buatier de Mongeot**

INFM, Unità di Genova and Dipartimento di Fisica, Università di Genova, Via Dodecaneso, 33-16136 Genova, Italy

E-mail: valbusa@fisica.unige.it

Received 16 January 2002, in final form 23 April 2002
Published 22 August 2002
Online at stacks.iop.org/JPhysCM/14/8153

Abstract

Surface etching by ion sputtering can be used to pattern surfaces. Recent studies using the high-spatial-resolution capability of the scanning tunnelling microscope revealed in fact that ion bombardment produces repetitive structures at nanometre scale, creating peculiar surface morphologies ranging from self-affine patterns to 'fingerprint'-like and even regular structures, for instance waves (ripples), chequerboards or pyramids. The phenomenon is related to the interplay between ion erosion and diffusion of adatoms (vacancies), which induces surface re-organization. The paper reviews the use of sputter etching to modify '*in situ*' surfaces and thin films, producing substrates with well defined vertical roughness, lateral periodicity and controlled step size and orientation.

(Some figures in this article are in colour only in the electronic version)

1. Ion sandblasting

In 1956 Navez *et al* [1], by bombarding a glass surface with an ion beam of air, observed for the first time a curious phenomenon: the bombardment produced a new morphology depending mainly on the incidence angle θ of the ion beam. The results are reported in figure 1. Here a clean glass surface has been exposed for 6 h to the ion beam at incidence angles ranging from 30° to 80°. The surface is covered by wavelike structures (ripples) separated by distances ranging from 30 ($\theta = 80°$) to 120 nm ($\theta = 30°$), which are stable under ambient conditions after the ion bombardment is finished. For incident angles close to $\theta = 0°$ the ripples are perpendicular to the ion beam direction, while they rotate by 90° when the beam reaches the surface at grazing incidence. In contrast, when the bombardment is performed at normal incidence, one observes a regular structure formed by elements of a diameter of about 40 nm. The authors did not provide an accurate explanation at that time, but simply tried to find analogies with macroscopic phenomena such as the ripple structures formed by wind over a sand bed. Figure 2 shows pictures of ripples observed in an Australian desert (figure 2(a));

[1] Author to whom any correspondence should be addressed.

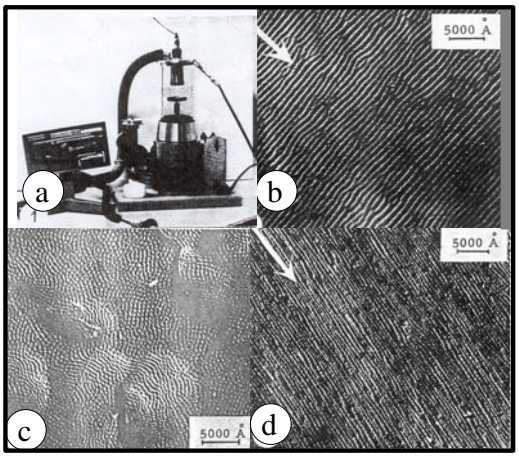

Figure 1. Experiment of Navez *et al* on glass [1] (SiO_2 72%; Al_2O_3 0.5%; Na_2O 13%; CaO 11%; MgO 3%). (a) An Azam ion gun working with air produces, with an acceleration voltage of 4 kV, an ion beam with an angular divergence $<10^\circ$ and a flux ranging from 0.5 to 2 μA mm^{-2}. (b) Glass surface after 6 h bombardment, $\theta = 30^\circ$. The arrow indicates the projection on the surface of the ion beam. The ripples align perpendicularly to the ion beam. (c) The same as (b) with $\theta = 0^\circ$, (d) the same as (b) with $\theta = 80^\circ$. The ripples align along the ion beam.

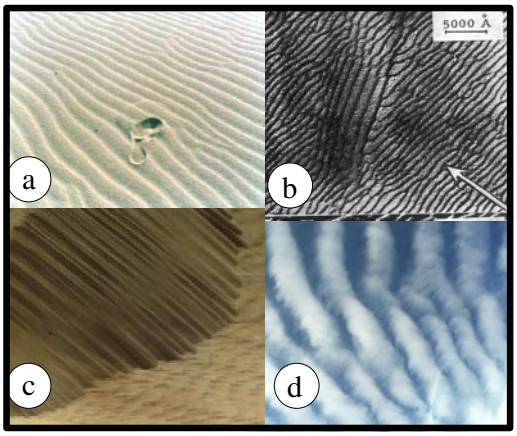

Figure 2. The same experiment as in figure 1 [1] compared with sand ripples observed in the desert. (a) Sand ripples on a dune in an Australian desert. (b) Glass surface after 6 h bombardment, $\theta = 45^\circ$. The arrow indicates the projection on the surface of the ion beam. The ripples align perpendicularly to the ion beam (arrow), but in the presence of an impurity they align parallel to the existing defect, which forms an angle of about 45° with the ripples. The effect is similar to that reported in (c) for the sand dune. (c) Sand ripples on a dune in a desert (Algeria). The ripples on the dune have different orientation with respect to the ripples in the open desert. (d) The clouds are the tops of the ripples between the dry, cool air above and the moist, warm air below.

they are very similar to the features observed on the glass modified by ion bombardment of figure 1. The formation of ripples on a sand dune occurs because the sand particles are so small that can behave like a fluid. Air and sand can be considered as two immiscible fluids moving at very different speeds. When air and sand come into contact, the boundary between them can develop complex wavelike structures and ripples form along the boundary. The wind

can pick up sand particles from the dune and move them around. If, by random chance, a small sand pile or a hollow forms somewhere, it will disrupt the airflow around it. The wind, forced to flow over or around the pile, slows down and can no longer carry as much sand with it, and it is therefore forced to deposit sand on the pile, which becomes larger and larger. The opposite occurs in the presence of a hollow. The wind increases its speed and sweeps more sand from the hollow. The entire process is unstable: the piles become larger and the hollows deeper. Eventually they form the ripples one can see on the dune. The similarities are very close even in anomalies, for instance the change in orientation in the presence of an obstacle. The sand ripples (figure 2(c)) align at the base of the dune as occurs in glass, where (figure 2(b)) in the presence of an impurity they align parallel to the existing defect. There are many other phenomena that produce similar patterns; for example strong similarities can be found in cumulus clouds on a partially sunny day. Figure 2(d) shows a picture of clouds: in this case the clouds are the tops of the ripples between the dry, cool air above and the moist, warm air below. The ion bombardment of a solid surface also looks very similar to the phenomenon of the sandblasting of solid surfaces [2], a method widely used for finishing metallic manufacturing. When a solid surface is eroded by a stream of abrasive particles a regular ripple pattern is created perpendicular to the surface component of the incident stream and with a wavelength comparable to the distance over which a single particle is in contact with the surface. The phenomenon recalls very closely the ion bombardment, where the erosion is produced by the 'abrasive' mechanism of the ion impinging on the surface. Even if the results are only qualitatively similar, the use of ion erosion for forming patterned surfaces is often called *ion sandblasting*. Nowadays, when the formation of periodic nanostructures is the key issue in the emerging field of nanotechnology, the understanding of the basic mechanisms of the ion sandblasting will allow us to extend the use of such a technique to a large variety of fabrication processes, allowing the *in situ* production of substrates with well defined vertical roughness, lateral periodicity and a controlled step size and orientation. The latter process can be defined as a sort of new lithography which is based on the re-organization of atoms and vacancies induced by ion bombardment, thus potentially opening new frontiers in the technology of thin films.

In section 1 the paper describes the erosion mechanism which is at the basis of the ion sandblasting, explaining the Bradley–Harper model (section 1.1), and reviews some of the experiments carried out on amorphous materials and semiconductors (section 1.2). In section 2, the paper focuses on the case of metals, where can be found two kinds of instability able to produce nanoscale patterning:

(i) the Erlich–Schwoebel barrier instability (section 2.1), which is dominant when the ion beam impinges at angles close to normal and at high substrate temperatures, and
(ii) the erosion instability (section 2.3), which induces pattern formation at low temperatures and grazing incident angles.

Section 2.4 describes the transition between the diffusive and erosive regimes. In section 2.2 the paper compares the mechanism of the ion erosion with the mechanism of homoepitaxial deposition. Section 3 concludes the paper, illustrating potential applications of the ion sandblasting.

1.1. Sigmund's theory of sputtering and the Bradley–Harper model

In 1988 Bradley and Harper [3] proposed a model for the ion sandblasting. Starting from Sigmund's [4] theory of sputtering, Bradley and Harper made a model (in the following referred to as the BH model), which explains why ion bombardment produces periodic height

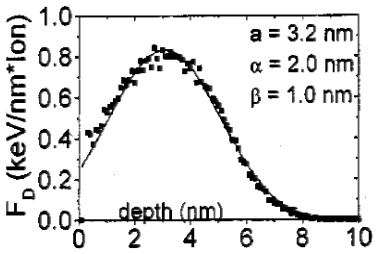

Figure 3. The damage–depth profile measured by Rutherford back-scattering compared with the Gaussian function of equation (1) for Xe^+ on HOPG(0001). Incident energy $E_i = 5$ keV and fluence $\Phi = 3 \times 10^{17}$ ions cm^{-2} as reported in [11].

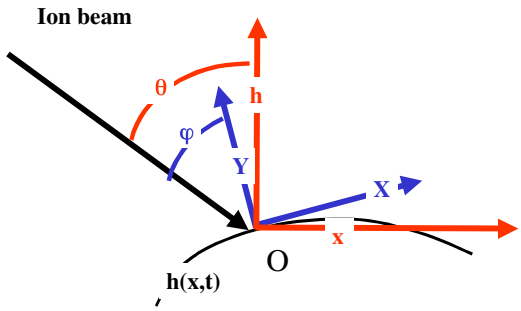

Figure 4. The reference coordinate systems used for a two-dimensional model.

modulations on the surface of amorphous solids. The rate at which the material is sputtered from a point O (see figure 4) of a surface is proportional to the power dissipated there by the random distribution of the incoming ions. They penetrate the surface and transfer their kinetic energy to the atoms of the substrate, which may start secondary collisions, thereby generating other recoiling atoms. A small fraction of the atoms is sputtered away, while some of them are permanently removed from their sites, making the substrate locally amorphous. In the limit of low energy of the incoming ions, the average energy deposited at O because of an ion penetrating into the crystal [5] follows the Gaussian:

$$E(r') = \frac{\varepsilon}{(2\pi)^{3/2}\alpha\beta^2} \exp[-(z')^2/2\alpha^2 - (x'^2 + y'^2)/2\beta^2] \tag{1}$$

where a is the mean range of ion penetration, α the longitudinal and β the lateral straggling width and ε the total energy deposited; a, α and β define the atomic collision cascade. A typical distribution of the implanted ions is reported in figure 3 for the case of Xe^+ on a freshly cleaved HOPG sample having (0001) orientation [6]. The figure illustrates the damage set profile as measured using Rutherford back-scattering compared with the Gaussian function of equation (1). The model calculates the normal component of the velocity of erosion at a generic point O of the interface when a uniform flux J hits the surface. The details are reported in [3]. Here we limit ourselves to reporting the most important steps. For simplicity let us reduce the model to a (1 + 1)-dimensional one as shown in figure 4. The incoming beam direction forms an angle φ with the direction normal to the surface Y. Y and the trajectory of the incoming ion beam form a plane containing the X-axis. We point out that φ changes from point to point along the surface. The radius of curvature at O is R_X (positive when the surface is concave

and negative when the surface is convex). The sputtering yields $Y(\varphi)$ is related to the velocity of erosion $v(\varphi, R_X)$ by the following expression:

$$Y(\varphi) = nv(\varphi, R_X)/J\cos\varphi \tag{2}$$

where n is the number of atoms per unit volume in the amorphous solid and J the flux of the incoming ions. Bradley and Harper have shown that equation (2) in the limit $a/R_x \ll 1$ can be approximated to the first order in a/R_x, giving the following expression for the erosion velocity:

$$v(\varphi, R_X) = \frac{J}{n}Y_0(\varphi)[\cos(\varphi) - \Gamma_X(\varphi)a/R_X]. \tag{3}$$

In equation (3) $Y_0(\phi)$ corresponds to the yield of a flat surface ($R_X = \infty$) and depends only on the parameters that define the collision cascade (a, ε, α, β) and on the angle φ. The expression of $Y_0(\varphi)$ deduced by Bradley and Harper is an increasing function of φ and therefore limits the model to angles not to close to grazing incidence, where the sputtering yield starts to decrease with φ. $\Gamma_X(\varphi)$ is a function of φ and of the parameters α and β. For $a = \alpha = \beta$, i.e. for a spherical distribution,

$$\Gamma_X(\varphi) = \sin^2(\varphi)\sin^2(\varphi/2) - \cos^2(\varphi/2). \tag{4}$$

The dependence of the erosion velocity on the curvature is in the term $\Gamma_X(\varphi)a/R_X$. For instance, for normal ion incidence $\Gamma_X(0)$ is negative, while the curvature is positive in the trough and negative in the crest; the product $\Gamma_X(0)a/R_X$ is negative in the trough and positive in the crest. The velocity of erosion is therefore faster for the trough than for the crest. Since $\Gamma(\varphi)_X$ is a continuous function, the surface is unstable against formation of periodic perturbations with k vector parallel to the surface component of the ion beam. The results are easily generalized [3] to arbitrary surfaces:

$$v(\varphi, R_X, R_Y) = \frac{J}{n}Y_0(\varphi)[\cos(\varphi) - \Gamma_X(\varphi)a/R_X - \Gamma_Y(\varphi)a/R_Y]. \tag{5}$$

Equation (3) can be transformed to the laboratory frame (x, h). h is the normal to the initial flat surface and $h(x)$ describes the surface. The ion beam forms with h an angle θ. The plane containing h and the ion trajectory identifies the x-axis. The time evolution of the surface is described by the height function $h(x, t)$ measured from the initial flat configuration and $\varphi = \theta + \frac{\partial h}{\partial x}$. θ is a fixed angle, while φ changes from point to point along the surface. The equation of motion is obtained by writing the normal component along h of the velocity of erosion, assuming that the surface height varies slowly. Equation (3) becomes

$$\frac{\partial h}{\partial t} = -\frac{J}{n}Y_0(\theta)\cos(\theta) + \frac{J}{n}\frac{\partial}{\partial\theta}[Y_0(\theta)\cos(\theta)]\frac{\partial h}{\partial x} + \frac{Ja}{n}Y_0(\theta)\left[\Gamma_x(\theta)\frac{\partial^2 h}{\partial x^2}\right] \tag{6}$$

where $v_0 = \frac{J}{n}Y_0(\theta)\cos(\theta)$ is the rate of erosion v_0 of the unperturbed planar surface. It is easy to generalize it to an arbitrary surface $h(x, y, t)$ [3]. After fixing the collision cascade parameters (α, β, ε, a) one obtains

$$\frac{\partial h}{\partial t} = -v_0(\theta) + \frac{\partial v_0(\theta)}{\partial\theta}\frac{\partial h}{\partial x} + \frac{Ja}{n}Y_0(\theta)\left\{\left[\Gamma_x(\theta)\frac{\partial^2 h}{\partial x^2}\right] + \left[\Gamma_y(\theta)\frac{\partial^2 h}{\partial y^2}\right]\right\}. \tag{7}$$

A more complete description of the effect incorporates the effect of self-diffusion [6], which generates a macroscopic current driven by the differences in the local chemical potential [7]. The equation also describing the relaxation effects induced by diffusion becomes

$$\frac{\partial h}{\partial t} = -v_0(\theta) + \frac{\partial v_0(\theta)}{\partial\theta}\frac{\partial h}{\partial x} + \frac{Ja}{n}Y_0(\theta)\left\{\left[\Gamma_x(\theta)\frac{\partial^2 h}{\partial x^2}\right] + \left[\Gamma_y(\theta)\frac{\partial^2 h}{\partial y^2}\right]\right\} + K\nabla^2\nabla^2 h + \eta(x, y, t) \tag{8}$$

where K is a coefficient which depends on the surface self-diffusivity D, the free energy per unit area γ and the number of atoms per unit area moving across the surface σ as

$$K = \frac{2D\gamma\sigma}{n^2 k_B T}. \tag{9}$$

$\eta(x, y, t)$ is a Gaussian white noise [8] with zero mean and variance proportional to the ion flux J, which takes into account the stochastic arrival of the ions.

In a more compact form equation (8) becomes

$$\frac{\partial h}{\partial t} = -v_0(\theta) + \frac{\partial v_0(\theta)}{\partial \theta}\frac{\partial h}{\partial x} + \nu_x(\theta)\frac{\partial^2 h}{\partial x^2} + \nu_y(\theta)\frac{\partial^2 h}{\partial y^2} + K\nabla^2\nabla^2 h + \eta(x, y, t) \tag{10}$$

where

$$\nu_x(\theta),\ \nu_y(\theta) \tag{11}$$

can change sign as the angle of incidence of the ion is varied. In this approach the local sputtering is caused by the random arrival of ions. The sputtering yield, depending on the surface gradient and curvature, generates surface roughening. The balance between the unstable erosion terms $-|\nu_x|\frac{\partial^2 h}{\partial x^2}$, $-|\nu_y|\frac{\partial^2 h}{\partial y^2}$ and the smoothing term $K\nabla^2\nabla^2 h$ generates ripples with a wavelength

$$\lambda_i = 2\pi\sqrt{2K/|\nu_i|} \tag{12}$$

where i refers to the direction (x or y) along which the associated $|\nu_i|$ is the largest. According to equation (10) the ripple orientation should be perpendicular to the beam direction (which is defined as the x direction of the surface) for incidence angle less than a critical value θ_c, and parallel to the beam direction for angles close to grazing.

1.2. Patterning amorphous materials

The BH model was very successful in predicting the ripple wavelength and orientation. There are many experiments performed on amorphous materials, which show the morphology predicted by the model. Very similar considerations apply for the case of single-crystal semiconductor surfaces, which upon ion impact become amorphized in the surface layers and thus lose the relationship with the high-symmetry directions of the bulk. A review on the use of ion sputtering on semiconductors appeared recently [9]. Apart from the early experiments on glass previously reported in figure 1, extensive work was carried out by several authors in the last decades. Ripples produced by off-normal ion scattering have been observed on SiO_2 [10], HOPG surfaces with (0001) orientation [11], diamond [12], Si [13–18], GaAs [19] and Ge [20]. A typical morphology is reported in figure 5, where the wavelength is shown as a function of incident angle. The sample, HOPG(0001), has been bombarded by Xe^+ at energy of 5 keV, and flux of 5 μA cm^{-2}. The sample has been exposed to an implantation fluence in the range 5×10^{16}–6×10^{18} cm^{-2}. The wavelength follows closely the prediction of the BH model. In figure 6 the experimental results are compared with the predictions of equation (12). The ripples are perpendicular to the ion beam direction for angles $\theta < \theta_c$ and parallel at grazing incidence in accord with the angular dependence of $\nu_x(\theta)$, $\nu_y(\theta)$. The wavelength does not depend on exposure time. The surface roughness as a function of the fluence is reported in figure 7 for the same samples. At low fluences Φ, w follows the prediction of the BH model with an exponential behaviour $w \propto \exp(\Phi)$. However, for fluences exceeding 10^{18} cm^{-2} the surface becomes self-affine and the wavepattern dissolves. In this limit, equation (10) does not describe the experiment. In order to include this effect in the model, it is necessary to take into account more terms in the development of the equation (5). Cuerno and Barabasi introduced nonlinear terms, with the coefficients depending on parameters such as the penetration depth and the angle of incidence [21]. In this way equation (10) becomes

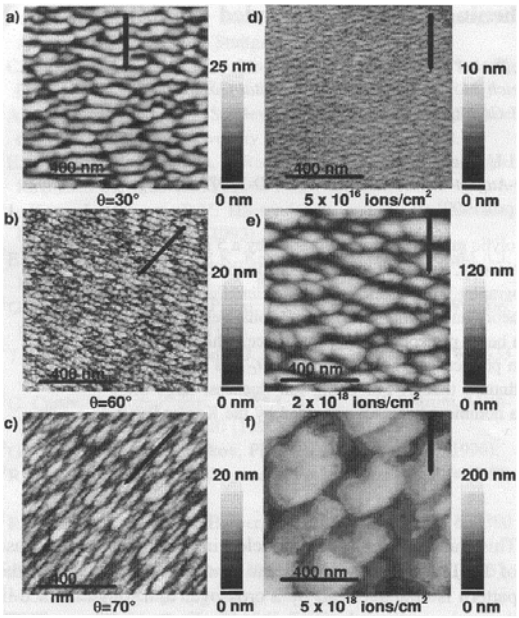

Figure 5. Eroded HOPG surfaces (lateral size 1 μm). Left column (a)–(c): irradiation fluence $\Phi = 3 \times 10^{17}$ cm^{-2}; incident angle θ (a) 30°, (b) 60°, (c) 70°. Right column (d)–(f): incident angle $\theta = 60°$; irradiation fluence (d) 5×10^{16}, (e) 2×10^{18}, (f) 5×10^{18} cm^{-2}. Arrows indicate the ion-beam orientation. From [11]

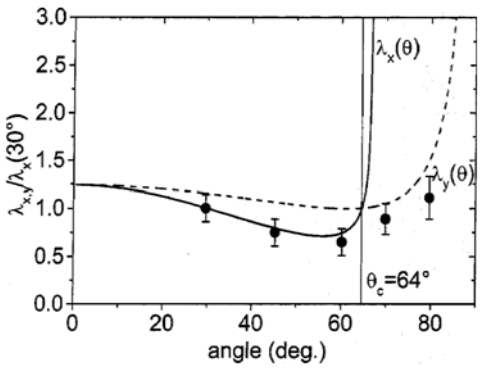

Figure 6. Xe^+-eroded HOPG surfaces from [11]. Continuous curve: angular dependence of the wavelength λ_x (ripples perpendicular to the ion beam direction) according to equation (12). Broken curve: angular dependence of the wavelength λ_y (ripples parallel to the ion beam direction) according to equation (12). The functions are normalized to $\lambda(30°)$.

$$\frac{\partial h}{\partial t} = -v_0(\theta) + \frac{\partial v_0(\theta)}{\partial \theta}\frac{\partial h}{\partial x} + \nu_x(\theta)\frac{\partial^2 h}{\partial x^2} + \nu_y(\theta)\frac{\partial^2 h}{\partial y^2} + \frac{\eta_x}{2}\left(\frac{\partial h}{\partial x}\right)^2 + \frac{\eta_y}{2}\left(\frac{\partial h}{\partial y}\right)^2 + K\nabla^2\nabla^2 h + \eta(x, y, t), \tag{13}$$

which belongs to the class of the anisotropic Kadar–Parisi–Zhang (KPZ) equations.

The scaling behaviour of equation (13) predicts two possible behaviours depending on the signs of η_x and η_y (for a detailed discussion of the effects induced by the presence of the non-linear terms see [21, 22]). Equation (13) also predicts a power law scaling for the roughness

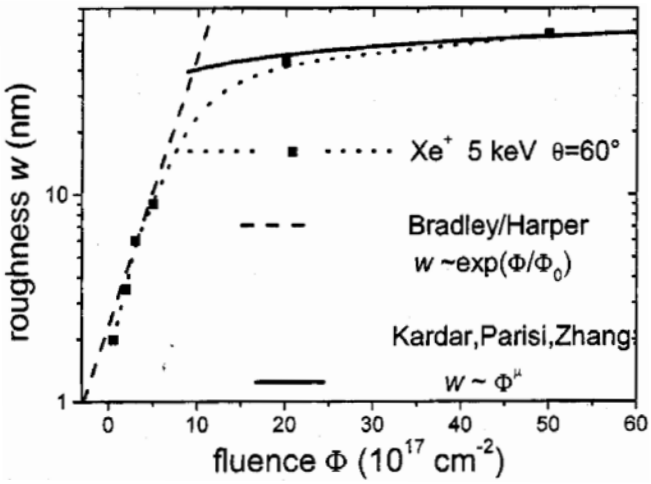

Figure 7. Dependence of the surface roughness w on fluence Φ. At low fluences the experiment follows the Bradley–Harper model, while at higher fluences the experiment fits the Kadar–Parisi–Zhang model (from [11]).

$w \propto \Phi^{\mu}$, which is actually observed in the experiment (see figure 7). In conclusion, for amorphous and semiconductor materials most of the experiments can be explained by using equation (10) or (13). Quite recently Umbach *et al* [23], studying ion-eroded SiO_2, proposed a model that takes into account the ion-assisted viscous relaxation in a thin surface layer, a process which has been shown to be the dominant smoothing process during erosion.

2. The case of metals

Particular attention should be devoted to the case of metals. Due to the higher diffusivity with respect to semiconductors and amorphous materials and to the non-directional character of the metallic bond, the ion impact does not imply the amorphization of the surface, at least for low ion fluences. The main effect associated with the impact of a single ion is the production of monatomic-height adatom and vacancy clusters [24], with a negligible build-up of point defects in the near-surface layers. Even after prolonged sputtering the crystalline quality of the substrate is not affected, as demonstrated by the observation that surface diffraction techniques can be used to determine the surface morphology [25–27]. In the case of metals, the build-up of a regular pattern is produced by two different mechanisms, which lead to a similar surface instability: the surface curvature dependence of the ion sputtering and the presence of an extra energy barrier whenever diffusing adatoms try to descend step edges. The effect was observed by Rusponi *et al* [28] on Ag(110) and later on Cu(110) [29, 30]. The results of [28] are reported in figure 8. Ar^+ ions with energy of 1 keV have been used to bombard Ag(110). The angle of incidence was set to normal, the temperature was varied in the range 150–400 K, the ion flux was 0.035 ML s^{-1} (1 ML corresponds to the atom surface density, equal to 8.44×10^{14} atoms cm^{-2} in Ag(110)) and the exposure time was 15 min. At low temperature (figure 8(a)) the surface is rough, without any evidence of organization. At $T = 230$ K (figure 8(b)) a ripple structure appears with the crests aligned along $\langle 001 \rangle$. At higher temperatures the structure evolves first into an array of rectangular mounds (figure 8(c)); for even higher temperatures a ripple structure aligned along $\langle 1\bar{1}0 \rangle$ is formed (figures 8(d),

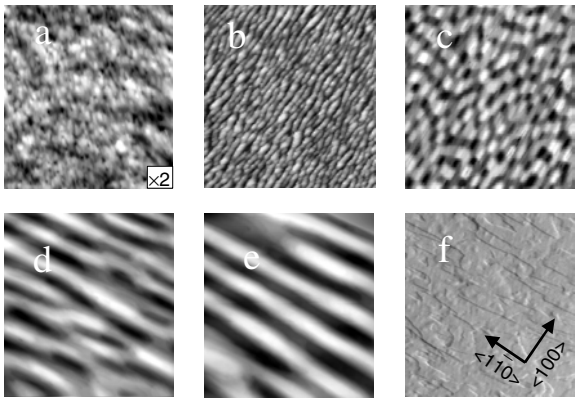

Figure 8. Six images (size 350 × 350 nm^2) of Ag(110) after ion sputtering ($J = 4$ μA cm^{-2}, $t = 15$ min, $\theta = 0^\circ$) for different temperatures. (a) 160 K; (b) 230 K; (c) 270 K; (d) 290 K; (e) 320 K; (f) 350 K.

(e)). At the highest temperature explored (figure 8(f)), the surface tends to smooth, loosing the ripple morphology. The structures produced in this case have a different nature from those observed on semiconductors or insulators and reported in the previous paragraph. In fact,

(a) they are created by bombardment at normal incidence, while this condition does not allow the formation of ripples on non-metal substrates,
(b) the ripple orientation depends on temperature,
(c) the ripple wavelength depends on temperature and
(d) the ripple wavelength depends on ion fluence.

In Ag(110) and Cu(110) the anisotropic surface diffusion of adatoms and vacancies is responsible for the phenomenon. On these surfaces, the $\langle 1\bar{1}0\rangle$ direction (in-channel direction) represents an easy pathway for the movement of both species of defects in comparison with the $\langle 001\rangle$ (cross-channel) direction; the surface temperature, changing the relative magnitude between the two diffusion rates, plays the key role determining the ripple orientation. Figure 9 shows the behaviour of the surface roughness w (figure 9(a)), of the average separation between ripples Λ (figure 9(b)) and of the local slope m (figure 9(c)) as functions of T. These quantities have been obtained by the analysis of the images of figure 8. It is evident that along a given azimuthal orientation, the trend of Λ and m is interconnected. In other terms, the features observed seem to be related to the surface symmetry and to the diffusion processes which are active at the temperature considered.

Similar results have also been found on symmetric substrates such as Al(111) [31], Cu(111) [32], Au(111) [27] and Pt(111) [33, 34]. Figure 10 reports [33] some scanning tunnelling microscope (STM) images acquired after Xe^+ bombardment of Pt(111), a surface in which adatom/vacancy diffusion is isotropic [35]. The Pt removed is indicated in ML (1 ML corresponds to the atom surface density for Pt(111), which is equal to 1.5×10^{15} atom cm^{-2}), assuming a sputtering yield of five Pt atoms per Xe ion. Looking at the figure, it is evident that the vacancy islands produced by the bombardment reflect the hexagonal symmetry of the surface. After 2.1 ML, a relevant coarsening of the vacancy islands is already active: seven layers are exposed at the same time. Increasing the removed amount, large pits with the same symmetry are created, as shown in figure 10(f). The roughness (cf figure 2 of [33]) increases as a function of the sputtering time, following a power law $w \approx t^{\beta}$, with $\beta = 0.58$, and the average separation between pits follows a similar behaviour (cf figure 3 of [33]). In surfaces

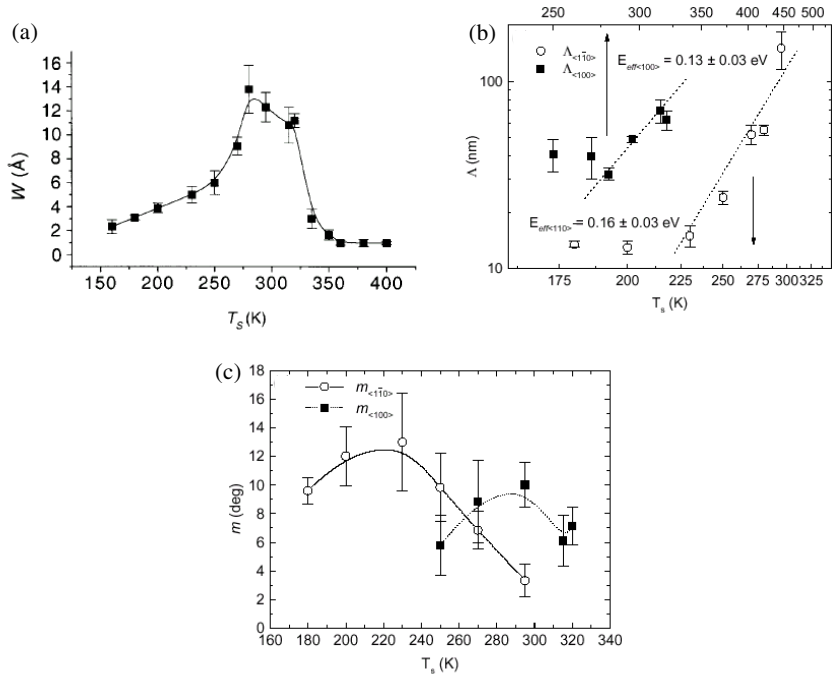

Figure 9. Ag(110) after Ar^+ sputtering; $J = 4\ \mu$A cm^{-2}, $t = 15$ min, $\theta = 0^\circ$. (a) Surface roughness w as a function of the substrate temperature; (b) ripple wavelength along $\langle 100\rangle$ and $\langle 1\bar{1}0\rangle$ as a function of temperature; (c) ripple slope along $\langle 100\rangle$ and $\langle 1\bar{1}0\rangle$ as a function of temperature. Curves connecting the experimental points have been plotted to guide the eye.

such as Ag(100) [36] squared pits replace the hexagonal ones, but the temperature behaviour is quite similar, as shown in figure 11. At low T (figures 11(a) and (b)) the sputtered surface appears rough, characterized by mounds, which become larger and larger with increasing T. At 350 K (figure 11(c)) well defined squared pits are present on the surface; their dimensions increase with temperature (figures 11(d) and (e)) and finally at 450 K (figure 11(f)) the surface is again flat, with few layers exposed. This temperature behaviour is explained in terms of different activation energies of the diffusion processes, which induce inter-layer mass transport. Both adatoms and vacancies contribute to the formation of the pits. The roughness, average separation and local slope as functions of the temperature are reported in figure 12. The surface roughness reaches a maximum in the range 325–400 K, and at the same temperatures there is a change in the local slope, which saturates around 22° at low T; the average separation increases exponentially with T and an activation barrier of 0.13 eV is found for temperatures >325 K. Similar results on surfaces with a square symmetry have been found on Cu(100) [37, 38].

In conclusion, diffusive processes are mainly responsible for the formation of regular structures on metal surfaces under ion bombardment; however, the temperature hierarchy of these processes cannot explain all observations if another source of instability is not considered in the model.

2.1. The Ehrlich–Schwoebel barrier and Villain's instability: the diffusive regime

The continuum model of equation (8) does not explain all the phenomena observed, since the contribution of the diffusive term $K\nabla^2\nabla^2 h$ is oversimplified. A simple correction to the

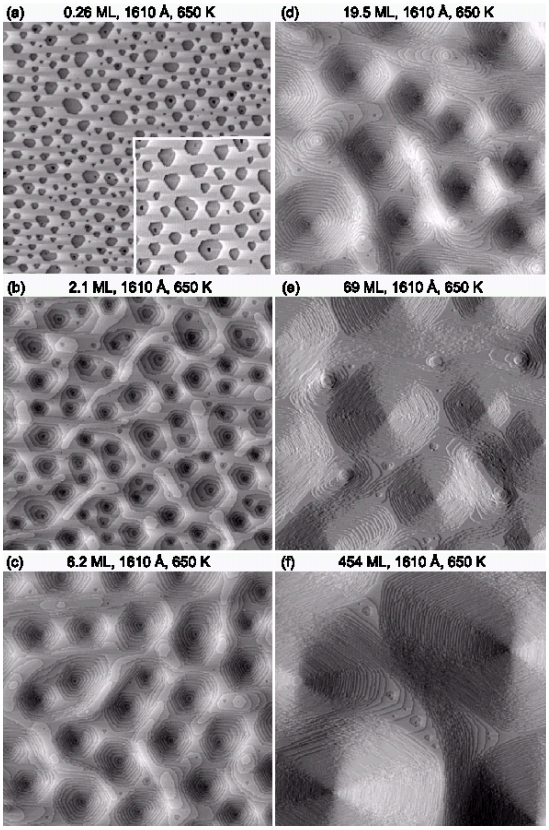

Figure 10. STM topographies after ion erosion of Pt(111) at 650 K. The removed amount is indicated. In the inset, a magnification of the initial stage (from [33]).

usual equation has been proposed in [30, 39] by introducing a different diffusion term for each principal surface direction and assuming that this term depends exponentially on temperature as

$$\frac{\partial h}{\partial t} = -v_0(\theta) + \frac{\partial v_0(\theta)}{\partial \theta}\frac{\partial h}{\partial x} + \nu_x(\theta)\frac{\partial^2 h}{\partial x^2} + \nu_y(\theta)\frac{\partial^2 h}{\partial y^2} - \sum_{\vec{n}}\left(D_{\vec{n}}\frac{\partial^4 h}{\partial \vec{n}^4} - S_{\vec{n}}\frac{\partial^2 h}{\partial \vec{n}^2}\right) + \eta(x, y, t). \tag{14}$$

The term $D_{\vec{n}}\frac{\partial^4 h}{\partial \vec{n}^4}$ takes into account the diffusion along the $\vec{n}$ crystallographic orientation and the term $S_{\vec{n}}\frac{\partial^2 h}{\partial \vec{n}^2}$ the contribution to the diffusion arising from the Ehrlich–Schwoebel barrier [40].

This model explains, at least qualitatively, the effects observed during the sputtering of metal surfaces. At normal incidence and low substrate temperatures, the '*erosion*' mechanisms alone would result in a rough and unstructured surface morphology, i.e. without the evidence of a ripple structure. However, the activation of the terrace diffusion barrier and of the Ehrlich–Schwoebel barrier opens the possibility for the development of the surface instability connected to ripple formation. By looking at the images of figure 8, and considering the hierarchy of inter- and intra-layer diffusion barriers, a hint at the mechanisms responsible for ripple rotation can be found. At low temperature (160 K), the surface is rough since the mobility of the adatoms (vacancies) is very low; at temperatures around 230 K, ripples appear along $\langle 001 \rangle$; the mobility sets in first along the $\langle 1\bar{1}0 \rangle$ troughs and the adatoms are not able to descend the steps because

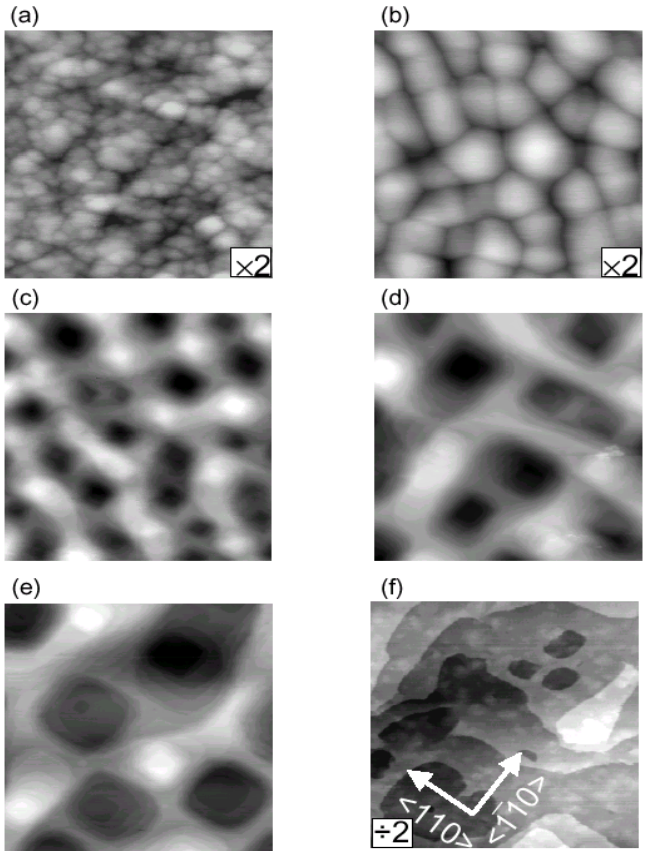

Figure 11. Six images (size 170 × 170 nm^2) of Ag(100) after ion sputtering ($J = 2.2\ \mu$A cm^{-2}, $t = 20$ min, $\theta = 0^\circ$) for different temperatures. (a) 130 K; (b) 250 K; (c) 350 K; (d) 380 K; (e) 400 K; (f) 450 K.

of the Erlich–Schwoebel barrier along that direction. As one increases the temperature to 270 K, the mobility also sets in along the ⟨001⟩ direction and the adatoms are also affected by the barrier along ⟨001⟩; instead of ripples, one now observes mounds, because the effect of the Erlich–Schwoebel barrier is present in both directions. At higher temperatures (290, 320 K) the adatoms can descend the steps first along ⟨1$\bar{1}$0⟩ and then along ⟨001⟩ and ripples are formed only along ⟨1$\bar{1}$0⟩. When the temperature is high enough (above 350 K) adatoms can efficiently descend the steps along ⟨1$\bar{1}$0⟩ and ⟨001⟩, and the surface becomes smooth and loses the ripple structure.

2.2. Sputtering versus deposition

If the formation of patterns on metal surfaces induced by ion sputtering is dominated by the diffusion processes of defects (adatoms and vacancies), a question arises: is it possible to induce the same structures by choosing the right deposition conditions in a growth experiment? In order to answer this question Buatier *et al* [41] deposited Ag on Ag(110) following the morphology with high-resolution electron diffraction (SPA-LEED). As reported in figure 13, in this case also the presence of regular structures is evident: at 130 K the two side peaks are

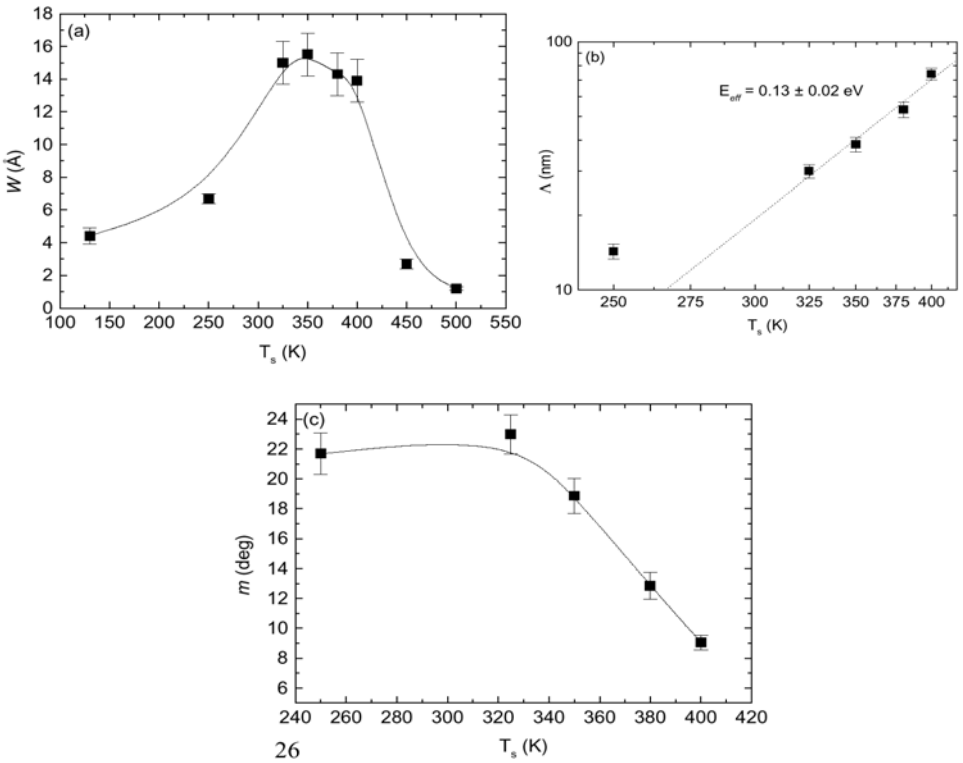

Figure 12. Ag(100) after Ar^+ sputtering; $J = 2.2\ \mu$A cm^{-2}, $t = 15$ min, $\theta = 0^\circ$. (a) Surface roughness w as a function of the substrate temperature; (b) ripple wavelength as a function of temperature; (c) ripple slope as a function of temperature. To make it easier to understand the graphics, curves connecting the experimental points have been plotted to guide the eye.

due to the formation of elongated features (ripples) oriented along the ⟨001⟩ direction, exactly what happens on the sputtered surface at low temperature (cf figure 8(b)). Increasing T, the symmetry of the diffraction pattern becomes fourfold, indicating that rectangular mounds are now present. At the end, ripples appear again at 210 K but rotated by 90° with respect to those observed at low T, in close analogy with the measurements made in the sputtering experiment. However, the temperature at which the rotation sets in is different between the two cases: about 170 K in growth and about 270 K in sputtering. This difference is explained [24] by taking into account the fact that in the growth experiment only adatoms are deposited on the surface, while the situation is more complicated in a sputtering experiment, where an ion hitting the surface creates both adatom and vacancy clusters, within about 2–3 nm around the impact site [24]. Then, the movement of these clusters requires a greater activation energy. This explains the 100 K temperature shift found in the sputtering experiments in comparison with the growth experiments.

The observation of surface morphologies such those of figures 10 and 11, where regular arrays of holes are formed after ion sputtering, would at first sight suggest that ion sputtering is equivalent to the deposition of vacancies instead of adatoms; this rough approximation is often used in computer simulations of the erosion process and in the interpretation of experimental data [42, 43]. However, this hypothesis is correct only if the temperature is high enough, as demonstrated in Ag(001) [24]. In this study the surface morphology obtained by ion sputtering

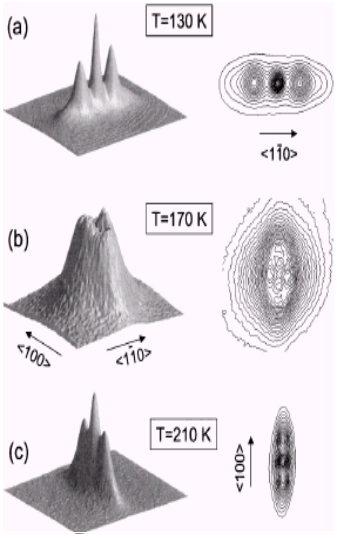

Figure 13. Two-dimensional SPA-LEED profiles centred at the specular (00) LEED beam, measured for near-in-phase diffraction conditions, after evaporation of 30 ML of Ag at a flux of 1 ML min^{-1}. The deposition temperatures are (a) 130 K, pattern size 42% BZ, $S = 1.9$; (b) 170 K, pattern size 27% BZ, $S = 1.84$; (c) 210 K, pattern size 27% BZ, $S = 1.88$. Left side: three-dimensional representations using a linear scale for the diffracted intensity. Right side: two-dimensional contour plots of the diffracted intensity. The arrows refer to the direct space surface orientations and have a length of 10% BZ. From [53].

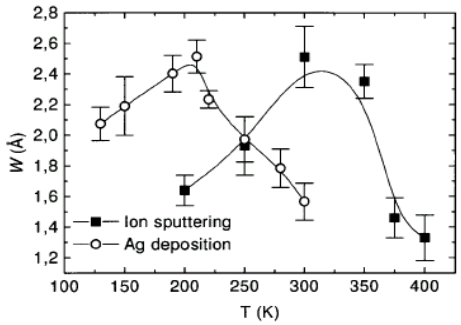

Figure 14. Temperature dependence of the surface roughness w for ion sputtering (full squares) and homoepitaxial deposition (open circles) on Ag(001). The experimental error bars show the statistical uncertainties derived from averaging over a large set of STM topographies. From [24].

and by deposition are compared. In order to make the comparison more meaningful, the atom deposition rate was chosen to be equivalent to the rate of total displacement of material during sputtering and, in particular, the ion flux used in sputtering was scaled down with respect to the deposition flux by the total number of atomic defects created in each ion impact. This number has been fixed at 35, as derived from the inspection of the damage produced by a single ion impact. In both experiments the surface was exposed for the same time ($t = 450$ s, corresponding to a nominal deposition of 33 monolayers) to the ion or atom beam and, immediately after turning off the particle source, the surface temperature was rapidly quenched to 130 K in order to avoid subsequent surface restructuring. In figure 14 the

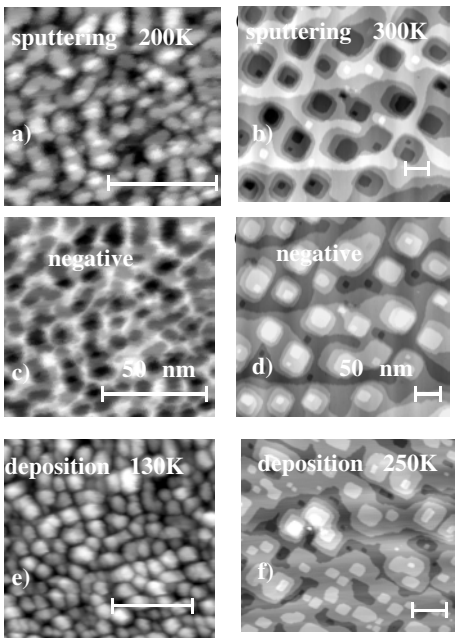

Figure 15. Grey-scale images representing the Ag(001) surface after Ne^+ sputtering (top row) and Ag deposition (bottom row) at low temperatures (left column, scan area 40×40 nm^2) and high temperatures (right column, scan area 63×63 nm^2). The temperatures shown are such that the sputter-induced nano-structures in (a) and (b) have the same lateral extension as the corresponding homoepitaxy-induced ones in (e) and (f). Images (c) and (d) in the middle row are the 'photographic negatives' of the corresponding sputtering images (a) and (b). From [24].

interface roughness is reported as a function of the substrate temperature: both processes, ion sputtering and Ag deposition, induce an increase of the roughness which reaches a well defined maximum before decreasing again. This bell-shaped behaviour is however shifted in temperature by about 100 K, indicating that, as observed in the Ag(110) case, two different kinds of defect are responsible for the actual morphology. The value of the roughness at the maximum is about the same in both cases, confirming the initial guess on the re-scaling of the fluxes. Only at high temperature does ion sputtering correspond to deposition of vacancies. In figure 15, the surface morphology obtained by ion sputtering (first row) at two different temperatures is compared with that obtained by deposition (third row). In the second row, the authors digitally transformed the first row, in such a way that a valley is changed in a mound and vice versa. As evident, at low temperature ion sputtering and deposition produce quite similar interfaces, in which mounds are more or less regularly arranged on the surface. The negative image is very different from that obtained by deposition. In contrast, at high temperature the sputtered surface presents deep squared holes, which after the digital inversion seem quite similar to the mounds obtained by deposition. This is a clear demonstration that only at high temperature is ion sputtering similar to a vacancy deposition. Again, the explanation of this behaviour is in the temperature hierarchy of the diffusion processes for adatoms and vacancy clusters: at low temperatures both adatom and vacancy clusters are immobile, and the surface morphology is randomly rough. Increasing temperature, the mobility and coalescence of adatom clusters sets in first, so that the surface acquires a mounded morphology. For even higher temperatures the vacancy clusters are also able to diffuse and coalesce, so that larger

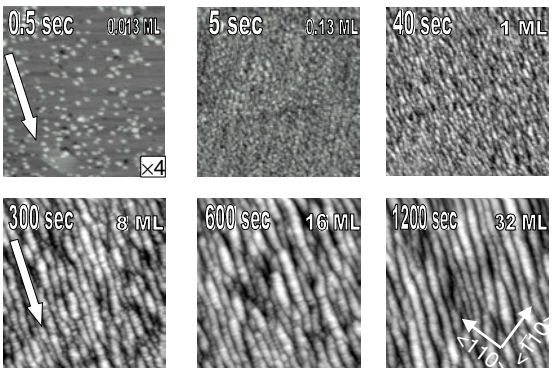

Figure 16. STM time sequence of an Ag(001) surface sputtered in the *erosive* regime. Ne^+ ions, $\theta = 70^\circ$, $T = 180$ K, $E_i = 1$ keV, $J = 5$ μA cm^2 (2.6×10^{-2} ML Ne^+ s^{-1}). Image size: 180×180 nm^2.

holes are able to develop, while the adatom clusters diffuse so fast that they are incorporated at the step edges, thus playing no role in the subsequent evolution of the surface morphology. At this point deeper and larger holes are able to grow.

2.3. The erosive regime in metals

The previous section showed that on single-crystalline metal surfaces it is possible to produce a regular array of nanostructures (chequerboard of square mounds on an fcc(001) substrate, hexagonal mounds on an fcc(111) surface or elongated ripples on an fcc(110) substrate) whose orientation is determined by the dominant diffusion direction; for this reason it is useful to call the set of conditions in which the nanostructures appear the '*diffusive*' regime. In this regime (normal incidence and high substrate temperatures) the diffusion of the produced adspecies (mainly clusters of adatoms and vacancies [24]) proceeds at a rate which is fast in comparison with the impingement rate of the ions, so the structure of the surface unit cell tends to be reflected in the orientation of the nanostructures (mounds or ripples), in particular with regard to the orientation of steps, which tend to be aligned along the thermodynamically preferred orientations. In the following this sputtering regime will be reported as the '*erosive*' regime, since the symmetry and orientation of the surface nanostructures is forced to be parallel to the ion beam orientation. The '*erosive*' sputtering regime is achieved only for grazing-incidence sputtering geometries (incidence angles θ approximately above 70°) and low substrate temperatures in order to inhibit thermally activated diffusion processes, which tend to smooth the surface and to orient the nanostructures along the preferential thermodynamic orientations [26, 30]. Figure 16 shows a sequence of STM images recorded at successive time intervals while sputtering on an Ag(001) substrate in the erosive regime ($T = 180$ K, $\theta = 70^\circ$). After the first stages of sputtering (0.013 ML Ne^+), the single-ion impact sites can be identified. As discussed in [24] the ion impact site is surrounded by clusters of adatoms and a central vacancy cluster. At temperatures around 180 K the mobility of the vacancy clusters is negligible as well as that of the adatom clusters, so as sputtering proceeds (0.13 ML Ne^+) the adatom clusters eventually coalesce. After a sputtering dose of 1 ML Ne^+ the first evidence of strong correlation is found and the symmetry of the surface nanostructures is not fourfold, as expected for a fcc(001) crystal termination, but twofold with the elongation of the nanostructures parallel to the ion-beam projection (arrow). For higher sputtering doses, 8, 16 or 32 ML, the coherence of the ripples increases as well as the number of exposed layers. The

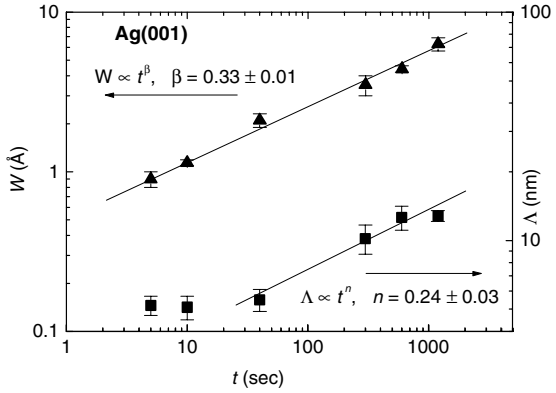

Figure 17. Time dependence of the surface roughness w (triangles) and the ripple separation Λ (squares) in the *erosive* regime for sputtering of Ag(001). $T_s = 180$ K, $E_i = 1$ keV Ne^+, $\theta = 70^\circ$, $J = 5\ \mu$A cm^{-2}.

interface width and the wavelength are found to follow a power law with time respectively as $W \propto t^\beta$ and $\Lambda \propto t^n$ as shown in figure 17. No evidence of saturation of either quantity is found after the longest sputtering time (30 min in the present experiments). By varying the sputtering time, it is possible to extend respectively the wavelength of the ripples in the range 5–12 nm and the interface width w in the range 0.1–0.8 nm. Such a power law behaviour with time is also found for sputtering in the erosive regime of other metal substrates such as Cu(110) and Ag(110). The erosive sputtering regime ($T = 180$ K, $\theta = 70^\circ$) produces surface structures which do not depend on the crystal type, symmetry or orientation as shown in figure 18. Figure 18(a) relates to an Ag(001) crystal; figure 18(b) refers to Cu(110), while figure 18(c) to Ag(110). Independent from the crystal type and orientation a comparable ripple wavelength of about 9 nm is obtained under similar sputtering conditions (Ar^+ or Ne^+, 2–5 μA cm^{-2}, 1 kV). It should be noticed that the difference in chemical identity of the projectile ions (Ne^+ in the case of Ag(001)) does not modify the wavelength of the ripples in comparison with the case of Ag(110) and Cu(110), where Ar^+ ions are used. A relevant fact which should be pointed out is that in the '*erosive*' sputtering regime a new degree of freedom is added compared with the *diffusive* sputtering regime or with the homoepitaxial growth experiments: this is given by the azimuthal orientation of the ion-beam projection. In figure 19 this statement is further demonstrated by a sequence of STM images of a Cu(110) substrate exposed to an ion beam under erosive conditions, parametric in the azimuthal orientation of the ion beam. Going from top to bottom, the ion-beam alignment switches from $\langle 1\bar{1}0\rangle$ to $\langle 001\rangle$ (arrow) and so does the orientation of the ripples, while no significant changes in the surface morphology (ripple wavelength, elongation or roughness) are noticed. This means that under *erosive* sputtering conditions it is possible to grow nanostructures which are aligned along thermodynamically unfavoured directions; such nanostructures cannot be grown by multilayer epitaxy or ion sputtering in the *diffusive* regime because there their step terminations are determined by the dominant diffusion energetic. In the case of Ag(001) (figures 16 or 18(a)), it is shown for example that an ion beam along $\langle 001\rangle$ forms ripples which expose predominantly $\langle 001\rangle$ steps, rather than the thermodynamically stable $\langle 1\bar{1}0\rangle$ termination.

A similar experiment, but for more grazing incidence angles ($\theta = 80^\circ$), was performed on a Cu(001) substrate [44], leading to results which bear similarities with the Ag(001) data of [24] i.e. the observation of ripples parallel to the ion beam direction, but also some noticeable

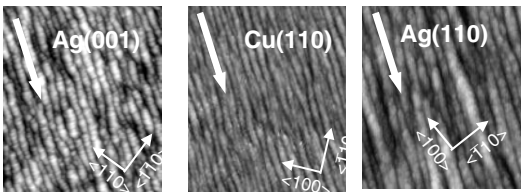

Figure 18. Sputtering in the *erosive* regime ($T = 180$ K, $\theta = 70^\circ$) of different substrates. (a) Ag(001), Ne^+ ions, $E_i = 1$ keV, $J = 5\ \mu$A cm^{-2}, $t = 10$ min; (b) Cu(110), Ar^+ ions, $E_i = 1$ keV, $J = 4.5\ \mu$A cm^{-2}, $t = 8$ min; (c) Ag(110), Ar^+ ions, $E_i = 1$ keV, $J = 3\ \mu$A cm^{-2}, $t = 10$ min. Image size: 180×180 nm^2.

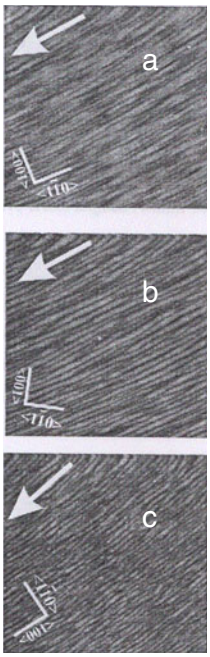

Figure 19. Grazing-incidence sputtering of Cu(110) in the *erosive* regime parametric in the azimuthal orientation of the ion beam. Independently of the crystal orientation, the ripples always develop along the ion-beam direction. Ar^+ ions, $\theta = 70^\circ$, $T = 180$ K, $E_i = 1$ keV, $J = 5\,\mu$A cm^{-2}, $t = 15'$. Image size 400×400 nm^2.

differences. For example, Cu(001) shows a dependence of the ripple wavelength on substrate temperature in the range 200–300 K [44] while for Ag(001) at $\theta = 70^\circ$ no dependence of wavelength is found up to 250 K (see the following figure). Moreover, in the case of Cu(001) sputtering, the ripple wavelength is found to depend linearly on the energy of the impinging ions in the range 0.2–2 keV, which was not explored in the Ag experiment. Another difference between the two experiments can be found in the number of exposed layers, which in the Ag case ($\theta = 70^\circ$) can reach values of about ten, with the formation of extended facets clearly visible in the diffraction pattern, while in the case of Cu ($\theta = 80^\circ$) only a couple of layers are exposed and no facets are formed on the sides of the ripples. Though no direct experimental evidence is provided in the Cu(001) experiment [44], these differences are most probably related to the way energy is released following a single ion impact at very grazing conditions, where single vacancies are supposed to be formed [44]. In the Ag case instead, as demonstrated in [24], a

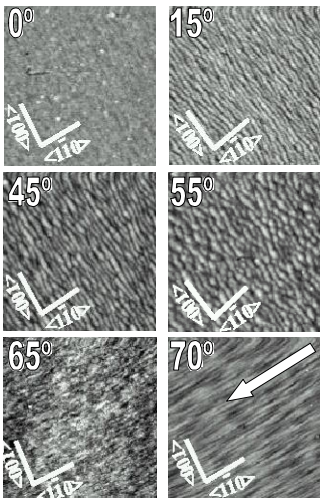

Figure 20. The role of the incidence angle θ in the transition from the *diffusive* to the *erosive* sputtering regime for Cu(110) at $T = 180$ K. The white arrow shows the ion-beam scattering plane. For all images, Ar^+ sputtering at $E_i = 1$ keV, $J = 5$ μA cm^{-2}, $t = 15'$. Image size 400×400 nm^2.

direct STM analysis of single ion impacts reveals that clusters of vacancies and adatoms are formed which have a reduced mobility compared with that of mono-vacancies and adatoms.

2.4. The transition between erosive and diffusive regimes

Figure 20 reports the case of Cu(110) when the transition between the diffusive and erosive sputtering regimes is achieved by an increase of the polar scattering angle of the ion beam, keeping the other experimental parameters, i.e. the ion flux, the ion energy and substrate temperature, fixed. Going from top to bottom, i.e. for increasing incidence angles, we can see that up to about $\theta = 55^\circ$ the ripples grow parallel to the $\langle 001 \rangle$ azimuth (the low-temperature orientation of the 'diffusive' ripples of Cu(110)—see [45]). For the present sputtering conditions a transition angle can be defined around $\theta = 55^\circ$–65° where no well defined ripple orientation is adopted due to the competition between diffusion, which tends to align the nanostructures along $\langle 001 \rangle$, and ion erosion, which forces the ridges to run parallel to the beam orientation (in this case along $\langle 1\bar{1}0 \rangle$). Already for $\theta = 65^\circ$ a certain degree of alignment of the ripples along the ion beam direction (in this case $\langle 1\bar{1}0 \rangle$) is observed, but after an increase of only 5° to $\theta = 70^\circ$ the coherence of the nanostructures becomes much stronger as well as the elongation and the aspect ratio. The existence of a transition angle around 60° for the switch between '*diffusive*' and '*erosive*' sputtering regimes is a general feature found on single-crystal metal surfaces. In figure 21, for example, it can be seen that in the case of Ag(001) a very similar dependence on the ion incidence angle occurs. For angles below $\theta = 70^\circ$ (*diffusive* regime) approximately square mounds are formed. Figures 21(a) and (b) are obtained by sputtering at $T = 180$ K, while in figures 21(c) and (d) the substrate temperature is $T = 250$ K, but this does not affect in a significant way the transition angle or the wavelength of the ripples, which is always around 10 nm. In the case of Ag and Cu, which have quite comparable diffusion barriers, important changes in the morphology of the surface nanostructures with temperature can be observed only for sputtering temperatures higher than 250 K. In figure 22 the effect of substrate temperature on the morphology of Ag(001) sputtered

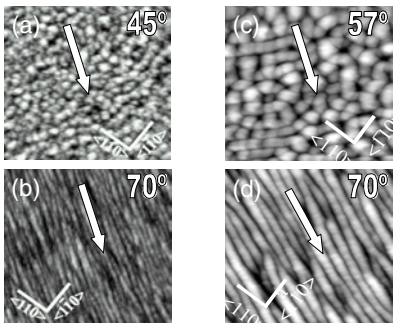

Figure 21. The role of the incidence angle θ in the transition from the *diffusive* to the *erosive* sputtering regime for Ag(001) at two different temperatures, $T = 180$ K (a), (b) and $T = 250$ K (c), (d). The white arrow shows the ion-beam scattering plane. Ne^+ ions, $E_i = 1$ keV, $J = 5\ \mu$A cm^{-2}, $t = 20'$. Image size: (a), (b) 310×310 nm^2, (c), (d) 180×180 nm^2.

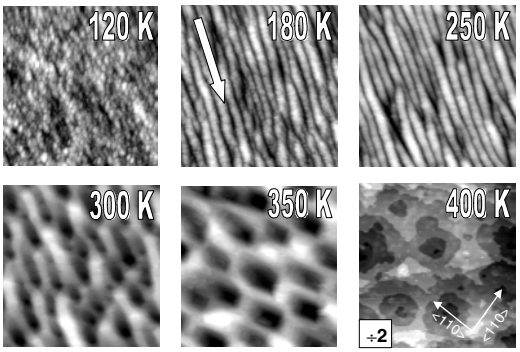

Figure 22. The role of surface temperature in the transition from the *diffusive* to the *erosive* sputtering regime for Ag(001). Ne^+ ions, $\theta = 70^\circ$, $E_i = 1$ keV, $J = 2.2\ \mu$A cm^{-2}, $t = 20'$. The white arrow shows the ion-beam scattering plane. Image size 180×180 nm^2; at $T = 400$ K 360×360 nm^2.

in the erosive regime is considered. The incidence angle is fixed, at $\theta = 70^\circ$, as well as the other external parameters, such as beam energy, ion flux and sputtering time, and we follow the change of surface morphology with sputtering temperature. For $T = 120$ K, a temperature at which essentially all the elementary diffusion processes are frozen, very little correlation is found among the small mounds which build up with sputtering, indicating that even in the so-called erosive regime, a limited amount of mobility of the defects is necessary to enhance the correlation between the adatom and vacancy clusters. At $T = 180$ K ripples elongated parallel to the ion-beam projection are obtained, and this situation is found up to $T = 250$ K, where the ripple coherence is even increased. Throughout this temperature range the ripple wavelength does not change in a significant way and stays fixed around 10 nm. At $T = 300$ K significant changes occur in the surface morphology, since the coalescence of the vacancy clusters appears to dominate the overall morphology, due to the enhanced mobility of the latter entities [46]. A residual correlation imposed by the ion-beam orientation can still be resolved, but now the action of surface diffusion, which tends to align the steps along the energetically favoured $\langle 1\bar{1}0\rangle$ orientations, becomes evident. This last statement is clear at $T = 350$ K, where a chequerboard of square vacancy mounds with edges aligned along $\langle 1\bar{1}0\rangle$ is formed which has no alignment with the ion beam. Now the diffusivity of the defects produced by the impinging

ions is so high on the timescale separating two successive impacts that the surface morphology is solely dictated by thermodynamic arguments (i.e. no strong dependence is found from the polar angle of the impinging ion beam even at grazing incidence). Finally at $T = 400$ K the surface diffusivity is so high (in particular with respect to the inter-layer channel) that the surface cannot develop well defined nanostructures.

2.5. Energy dependence

The dependence on ion energy of the separation of the periodic nanostructures formed by ion sputtering in the keV range was not the object of a deep study in the previous experiments on single-crystal metal surfaces. The experiments have shown that the nanostructures produced by sputtering in the diffusive regime show a periodicity which is weakly dependent on ion energy in the range 0.6–2 keV for the cases of Ag(110), Cu(110) and Ag(001). This can be understood considering that in the diffusive regime, thanks to the relatively high substrate temperatures and increased mobility, the defects produced after the ion impact (mostly adatom and vacancy clusters [24]) can adopt an equilibrium configuration by thermal diffusion, so that the final surface morphology is less dependent on dynamics of the single ion impact. This is consistent with the observations on the energy dependence of the adatom and sputter yields after single ion impacts on Pt(111) in the energy range 0.6–2 keV, where few variations have been found [47]. According to the above-mentioned study, in order to observe more pronounced changes in the adatom production yield, the impact energy should be reduced to the 100 eV range or above 5 keV for the heavier Ar and Xe ions (for the lighter Ne ions a saturation in the adatom yield appears to take place around 3 keV).

In the case of sputtering in the erosive regime, i.e. at grazing incidence and for low substrate temperature, since relaxation of the adatoms via thermal diffusion is less efficient, the differences in the single-ion-impact fingerprints with energy are expected to play a more important role in the final surface morphology. In the case of Cu(001) when ion incidence occurs at an angle $>80^\circ$ [44], very shallow grooves are formed parallel to the ion-beam projection. Below 200 K the wavelength of the grooves does not depend on temperature, while a linear increase of the wavelength from 4 to 10 nm is observed when the ion energy varies in the range 0.4–2.2 keV. Above 2 keV a deviation from the linear trend is observed, which could be attributed to a release of the ion energy over deeper areas, but no quantitative explanation of this observation is at the moment at hand.

We mention here that in the case of GaAs and InSb surfaces pattern formation with a hexagonal array of dots is observed after low-energy ion sputtering under normal incidence, which shows a peculiar dependence of the dot separation on ion energy. On GaSb and InSb surfaces the characteristic length is proportional to the square root of the ion energy over a large range of energies [48]. The energy dependence of the characteristic wavelength confirms predictions made by solutions of the linear continuum equation with an effective ion-induced diffusion as the dominant relaxation process for Ar ion energies of 75 –1800 eV and temperatures $<60\,^\circ$C. From the scaling of the characteristic length with ion energy the power-law dependence of the lateral width of the deposited energy with an exponent $2m$ with $m = 0.25$ is concluded.

3. Conclusions

The ‘ion sandblasting’ is not only interesting from a basic point of view, since it can help us for example to understand what diffusion processes are relevant on a metal at a fixed temperature, but the method is also quite intriguing since it can be used to modify in a simple way the surface

morphology and then other important properties. Until now, there have been few examples in the literature of the use of this method in order to build nanostructures or to modify surface properties. A typical example in this direction is the experiment of Fackso *et al* [49, 50]; with this method, the authors were able to prepare on a gallium antimonide surface a regular hexagonal lattice of dots of 35 nm in diameter, demonstrating that the method can be useful in device fabrication. With a similar approach ordered silicon nanostructures has been produced by ion sputtering at normal incidence [15] and GaAs quantum dots have been grown on a Si nanopatterned template [51]. Vattuone *et al* [52] demonstrated that the capability to control the step density and orientation can have important applications in the field of surface catalysis. There it was shown that on an Ag(001) substrate patterned as in figure 16, thanks to the high reactivity of the ⟨001⟩ steps towards oxygen dissociation, it is possible to tune the reactivity by orders of magnitude compared with a flat substrate.

In summary, in previous sections we have shown that the use of ion etching allows production of regular surface patterns on a nanometre scale. In the '*diffusive*' sputtering regime, by tuning the competition between erosion- and diffusion-induced surface re-organization, it is possible to investigate new phenomena such as the rotation of ripple orientation on an anisotropic fcc(110) substrate and the patterning of an fcc(001) substrate from moundlike to ripple structure. Surface morphologies similar to ones obtained in the '*diffusive*' sputtering regime are found in the case of homoepitaxial growth on both anisotropic and isotropic substrates. The general approach considers sputtering as the negative of homoepitaxial deposition, i.e. as a deposition of vacancies, which can eventually have an asymmetry in their diffusivities. This picture is oversimplified because in the energy regime explored in the present study the dominant effect of noble gas ion sputtering on metal surfaces is the formation of clusters of adatoms and vacancies. By sputtering in the so-called '*erosive*' regime, i.e. for grazing-ion-incidence conditions and low substrate temperature, the surface nanostructures are forced to grow parallel to the ion-beam projection. This new degree of freedom, which is not accessible in the case of homoepitaxial growth or for sputtering in the '*diffusive*' regime, opens up the possibility to pattern the surface along non-thermodynamic orientations. The possibility to force the growth of the nanostructures along desired orientations was exploited in [26] to obtain either a chequerboard of square mounds or a ripple structure on an isotropic substrate such as Ag(001) by controlling either the sputtering temperature or the sputtering angle.

References

[1] Navez M, Sella C and Chaperot D 1962 *C.R. Acad. Sci., Paris* **254** 240
[2] Carter G, Nobes M J, Paton F, Williams J S and Whitton J L 1977 *Radiat. Eff.* **65** 33
[3] Bradley R M and Harper J M E 1988 *J. Vac. Sci. Technol.* A **6** 2390
[4] Sigmund P 1965 *J. Mater. Sci.* **8** 1545
[5] Sigmund P 1969 *Phys. Rev.* **84** 383
[6] Herring C 1950 *J. Appl. Phys.* **21** 301
[7] Barabasi A L and Stanley H E 1995 *Fractal Concepts in Surface Growth* (Cambridge: Cambridge University Press)
[8] Eklund E A, Snyder E J and Stanley Williams R 1993 *Surf. Sci.* **285** 157
[9] Carter G 2001 *J. Phys. D: Appl. Phys.* **34** R1
[10] Mayer T M, Chason E and Howard A J 1994 *J. Appl. Phys.* **76** 1633
[11] Habenicht S 2001 *Phys. Rev.* B **63** 125419
[12] Datta A, Yuh-Renn Wu and Wang Y L 2001 *Phys. Rev.* B **63** 125407
[13] Carter G, Vishnyakov V and Nobes M J 1996 *Nucl. Instrum. Methods* B **115** 440
[14] Erlebacher J, Aziz M J, Chason E, Sinclair M B and Floro J A 1999 *Phys. Rev. Lett.* **82** 2330
[15] Gago R, Vazquez L, Cuerno R, Varela M, Ballesteros C and Albella J M 2001 *Appl. Phys. Lett.* **78** 3316

[16] Chini T K, Datta D B S R and Sanyal M K 2001 *Appl. Surf. Sci.*
[17] Jiang Z X and Alkemade P F A 1998 *Appl. Phys. Lett.* **73** 315
[18] Vajo J J, Doty R E and Cirlin E 1996 *J. Vac. Sci. Technol.* A **14** 2709
[19] Datta D, Bhattacharyya S R, Chini T K and Sanyal M K 2001 *Nucl. Instrum. Methods*
[20] Chason E, Mayer T M, Kellerman B K, McIlroy D T and Howard A J 1994 *Phys. Rev. Lett.* **72** 3040
[21] Cuerno R and Barabasi A L 1995 *Phys. Rev. Lett.* **74** 4746
[22] Barabasi A L, Makeev M A, Lee C S and Cuerno R 1997 *Proc. 4th CTP Workshop on Statistical Physics*
[23] Umbach C C, Headrick R L and Chang Kee-Chul 2001 *Phys. Rev. Lett.*
[24] Costantini G, Buatier De Mongeot F, Boragno C and Valbusa U 2001 *Phys. Rev. Lett.* **86** 838
[25] Buatier de Mongeot F, Costantini G, Boragno C and Valbusa U, submitted
[26] Rusponi S, Costantini G, de Mongeot F B, Boragno C and Valbusa U V 1999 *Appl. Phys. Lett.* **75** 3318
[27] Ramana Murty M V, Curcic T, Judy A, Cooper B H, Woll A R, Brock J D, Kycia S and Headrick R L 1999 *Phys. Rev.* B **60** 16 956
[28] Rusponi S, Boragno C and Valbusa U 1997 *Phys. Rev. Lett.* **78** 2795
[29] Rusponi S, Boragno C and Valbusa U 1998 *Phys. Low Dim. Struct.* **12** 55
[30] Rusponi S, Costantini G, Boragno C and Valbusa U 1998 *Phys. Rev. Lett.* **81** 2735
[31] Busse C, Engin C, Hansen H, Linke U, Michely T and Urbassek H M 2001 *Surf. Sci.* **488** 346
[32] Naumann J, Osing J, Quinn A J and Shvets I V 1997 *Surf. Sci.* **388** 212
[33] Kalff M, Comsa G and Michely T 2001 *Surf. Sci.* **486** 103
[34] Strobel M, Heinig K H and Michely T 2001 *Surf. Sci.* **486** 136
[35] Michely T and Comsa G 1991 *Surf. Sci.* **256** 217
[36] Costantini G, Rusponi S, Gianotti R, Boragno C and Valbusa U 1998 *Surf. Sci.* **416** 245
[37] Ritter M, Stindtmann M, Farle M and Baberschke K 1996 *Surf. Sci.* **348** 243
[38] Ernst H J 1997 *Surf. Sci.* **383** L755–9
[39] Costantini G, Rusponi S, de Mongeot F B, Boragno C and Valbusa U 2001 *J. Phys.: Condens. Matter* **13** 5875
[40] Politi P and Villain J 1996 *Phys. Rev.* B **54** 5114
[41] Buatier de Mongeot F, Costantini G, Boragno C and Valbusa U 2000 *Phys. Rev. Lett.* **84** 2445
[42] Teichert C, Ammer C and Klaua M 1994 *Phys. Status Solidi* a **146** 223
[43] Murty R M V, Curcic T, Judy A, Cooper B H, Woll A R, Brock J D, Kycia S and Headrick R L 1998 *Phys. Rev. Lett.* **80** 4713
[44] Van Dijken S, de Bruin D and Poelsema B 2001 *Phys. Rev. Lett.* **86** 4608
[45] Rusponi S, Costantini G, Boragno C and Valbusa U 1998 *Phys. Rev. Lett.* **81** 4184
[46] Erlebacher J, Aziz M J, Chason E, Sinclair M B and Floro J A 1999 *Phys. Rev. Lett.* **82** 2330
[47] Michely T and Teichert C 1994 *Phys. Rev.* B **50** 11 156
[48] Facsko S, Kurz H and Dekorsy T 2001 *Phys. Rev.* B **63** 165329
[49] Facsko S, Bobek T, Dekorsy T and Kurz H 2001 *Phys. Status Solidi* b **224** 537
[50] Facsko S, Dekorsy T, Koerdt C, Trappe C, Kurz H, Vogt A and Hartnagel H L 1999 *Science* **285** 1551
[51] Li G, Zhang J, Yang L, Zhang Y and Zhang L 2001 *Scr. Mater.* **44** 1945
[52] Vattuone L, Burghaus U, Savio L, Rocca M, Costantini G, de Mongeot F B, Boragno C, Rusponi S and Valbusa U 2001 *J. Chem. Phys.* **115** 3346
[53] Costantini G, Buatier de Mongeot F, Boragno C and Valbusa U 2000 *Surf. Sci.* **459** L487